SCIENTIFIC REPORTS

OPEN

SUBJECT AREAS:
SOFT MATERIALS
MATERIALS CHEMISTRY

Received
7 October 2013

Accepted
17 December 2013

Published
14 January 2014

Correspondence and requests for materials should be addressed to H.M.Y. (hmyang@csu.edu.cn)

CuO nanoparticles encapsulated inside Al-MCM-41 mesoporous materials via direct synthetic route

Chengli Huo, Jing Ouyang & Huaming Yang

Department of Inorganic Materials, School of Resources Processing and Bioengineering, Central South University, Changsha 410083, China.

Highly ordered aluminum-containing mesoporous silica (Al-MCM-41) was prepared using attapulgite clay mineral as a Si and Al source. Mesoporous complexes embedded with CuO nanoparticles were subsequently prepared using various copper sources and different copper loadings in a direct synthetic route. The resulting CuO/Al-MCM-41 composite possessed *p6mm* hexagonally symmetry, well-developed mesoporosity, and relatively high BET surface area. In comparison to pure silica, these mesoporous materials embedded with CuO nanoparticles exhibited smaller pore diameter, thicker pore wall, and enhanced thermal stability. Long-range order in the aforementioned samples was observed for copper weight percentages as high as 30%. Furthermore, a significant blue shift of the absorption edge for the samples was observed when compared with that of bulk CuO. H_2-TPR measurements showed that the direct-synthesized CuO/Al-MCM-41 exhibited remarkable redox properties compared to the post-synthesized samples, and most of the CuO nanoparticles were encapsulated within the mesoporous structures. The possible interaction between CuO and Al-MCM-41 was also investigated.

Since the discovery of mesoporous molecular sieves (M41S) by scientists at Mobil Research & Development Corporation, the synthesis of ordered mesoporous materials (OMM) has been an active area of research because these materials have highly ordered channels and large surface areas[1–9]. Aluminosilicate M41S materials, such as Al-containing MCM-41 (Al-MCM-41), have been the focus of a significant amount of research because the tetrahedrally coordinated Al can produce active sites for adsorption, ion exchange and catalysis[10–12]. The structural integrity of Al-MCM-41 and related mesoporous aluminosilicate molecular sieves has been significantly improved through direct assembly and post-synthesis modification methods[13–15]. Previously, mesoporous aluminosilicates have been synthesized by utilizing post-synthetic treatments such as pore-wall grafting or recrystallization using various sources of aluminum[16–21]. This is possible due to the high density of silanol groups on the pore surface of MCM-41 to which guest species can be attached. However, post-synthetic routes utilize two steps that are generally performed in organic solvents, which will usually result in the formation of aluminum oxide or oxyhydroxide particles in the channels or on the external surface of the material. The formation of metal oxides in mesopores will fully or partially block the pores, therefore reducing surface area, pore volume, and pore diameter. These reductions can potentially affect the adsorption or catalytic properties of M41S materials[21,22]. It is therefore highly desirable to identify a direct synthetic route for the synthesis of MCM-41 materials where Al is incorporated into the framework to increase the acidity of the material without changing the material's structural order. Typically, directly synthesized aluminum containing mesoporous silica is prepared from a mixture of silicon and aluminum sources or by utilizing zeolite seeds as precursors for the assembly of mesostructures[5,13,15,23–25]. Alternatively, the use of a mixed-gel containing both a source of silicon and aluminum has been explored for the synthesis of ordered mesoporous aluminosilicates. The hybrid materials are obtained by in situ co-condensation[3,22,26]. Furthermore, recent studies have shown that ordered mesoporous aluminosilicates can also be synthesized in one step by utilizing a single source molecular precursor and templating micella[27,28]. This direct method typically results in a relatively homogeneous incorporation of the Al, and the aluminum species are generally tetrahedrally coordinated to oxygen atoms that form covalent bridges to neighboring tetrahedral silica.

Recently, the preparation of mesoporous materials that are derived from various types of natural layered silicates (such as saponite, bentonite, metakaolin, and talc) has been emphasized because of the abundance of the starting material and the similarity of the natural material's structure units to those of mesoporous

materials[29–34]. We also successfully synthesized the hexagonally ordered aluminum-containing mesoporous silica (Al-MCM-41) from natural attapulgite and the necessary pretreatment processes that involve mechanical grinding and acid leaching[35]. These aluminosilicate-mesoporous materials derived from layered silicates have a high-specific surface area, pore volume, and hydrothermal stability. These characteristics indicate that these materials can potentially be used as heterogeneous catalysts[36]. On the other hand, the encapsulation of inorganic species into mesoporous silica can produce regular nanoparticles with a well-controlled particle size and distribution, and therefore, this area of research currently receives significant attention[37]. Two approaches, direct synthesis (co-condensation reaction) and post-synthesis reaction (grafting), have been widely investigated to prepare hybrid OMMs[38]. To date, numerous attempts have been made to synthesize nanoparticles that are encapsulated inside mesoporous silica, mainly focused on semiconductors[39–41], metal oxides[34,42–46], and transition metals[47–52]. These nanoparticles are incorporated into mesoporous materials through a post-synthetic reaction that utilizes the high concentration of silanol groups on the surface of mesoporous silica, which can act as anchoring sites for guest species[53]. However, this method mainly utilizes a number of processes such as sorption, ion-exchange, complexation, and covalent grafting. A general disadvantage inherent to these methods is the unavoidable adsorption of the inorganic precursors on the external surface of the mesoporous silica. This adsorption leads to the growth of large particles outside the mesopores that severely weaken the desired properties of the material[37]. To overcome these disadvantages, multiple efforts have been devoted to the development of direct synthetic routes, and it has been demonstrated to be an efficient approach to prepare ordered mesoporous silica with guest species encapsulated inside the channels of the material. In contrast to previously reported multistep processes for synthesizing mesoporous silica and nanoparticles separately, highly ordered mesoporous silica monoliths and nanocrystals can be obtained simultaneously in controllable quantities. Recently, it has been reported that a large number of guest species are incorporated into OMMs synthesized using direct synthesis[54–59]. The greatest advantage of direct synthesis is that it produces materials with high loadings and relatively uniform distributions of the functional groups[38].

Copper oxide (CuO), a p-type semiconductor with a narrow band gap (E_g = 1.2 eV), has attracted significant attention because of its diverse applications as a semiconductor, organic catalyst, gas sensor, and lithium ion electrode material[60,61]. CuO has been widely used as a heterogeneous catalyst in many important chemical processes, including the degradation of nitrous oxide, the selective catalytic reduction of nitric oxide with ammonia, and oxidations of carbon monoxide, hydrocarbons, and fine chemicals[62]. Some researchers have introduced CuO nanoparticles into mesoporous silica; in most cases, organic reagents were utilized as the Si sources[58,59], and few reports have focused on utilizing a healthy and green Si source.

In this paper, we reported a synthetic route to aluminum-containing hexagonally ordered mesoporous silica (Al-MCM-41) from natural attapulgite without the addition of silicon or aluminum reagents. Additionally, a facile and effective direct synthetic method for the production of Al-MCM-41 capsules with CuO nanoparticles was proposed. In this method, an amino-Cu complex may be formed prior to silica polymerization. Subsequent template removal produced copper-oxide-encapsulating mesoporous composites with a relatively high specific surface area. In this synthetic method, CuO was directly placed into the pores and expected to be available at higher loadings of metal oxide. In addition, the encapsulation process described in this paper is versatile and convenient, and it can be extended to a broad range of guest species such as metal oxides and metals. The mesoporous composites have broad potential applications in environmentally relevant fields such as catalysis and gas separation.

Results

Small-angle XRD patterns of the as-synthesized and calcined Al-MCM-41 (Figure 1A(a,b)) in $2^\circ < 2\theta < 10^\circ$ both show four well-resolved peaks that can be indexed to (100), (110), (200) and (210) reflections associated with a *p*6 mm hexagonal symmetry. After calcination, the four diffraction peaks of the as-synthesized sample are shifted to higher diffraction angles; therefore, calcination produces condensation of the framework. Calculation of the lattice constant α_0 gives a value of 4.54 nm, which is close to the value of 4.81 nm recorded for Al-MCM-41 prepared using a CTAB template with attapulgite as a source of both Si and Al[35]. Three peaks can be observed in Figure 1A(c), indicating the host structure of the well ordered mesoporous Al-MCM-41 is well maintained after the encapsulation of CuO nanoparticles inside its matrix. Wide-angle XRD patterns (Figure 1B(a,b)) of the as-synthesized and calcined sample both exhibit one broad peak from 20° to 23° which can be ascribed to amorphous silica, whereas the CuO/Al-MCM-41 (Figure 1B(c)) shows the (002), (111), and ($\bar{2}$02) diffractions of CuO in the range of $30^\circ < 2\theta < 50^\circ$, supporting the presence of CuO nanoparticles on the mesostructures.

Transmission electron microscopy (TEM) analysis indicates that the highly ordered structure is retained after the calcination process

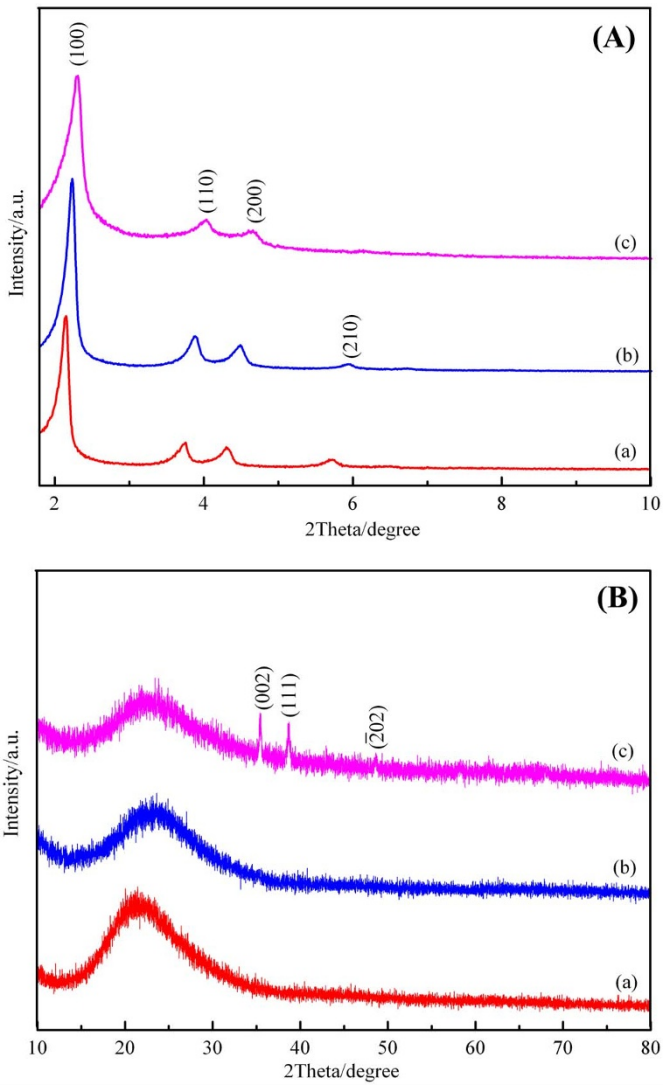

Figure 1 | Crystallization of the samples. (A) small-angle XRD and (B) wide-angle XRD patterns of the samples (a) as-synthesized, (b) calcined Al-MCM-41 samples, (c) direct-synthesized CuO/Al-MCM-41.

(Figure 2), representative TEM images of the calcined Al-MCM-41 with a highly ordered hexagonal structure can be clearly observed in the image taken with the electron beam parallel to the pore direction (Figure 2a). Additionally, the micrograph that was taken with the electron beam perpendicular to the pores shows both the channels and the framework (Figure 2b). These results clearly demonstrate that the final product Al-MCM-41 is a highly ordered mesoporous material with long-range order and a regular two-dimensional hexagonal pore structure. Figure 2c,d also show the hexagonal-ordered pore structures of the direct-synthesized CuO/Al-MCM-41 samples, which can be clearly evidenced by the remained ordered mesostructure of the silica monoliths after the incorporation of the CuO particles into the pores of Al-MCM-41. In addition, there is no evidence of the formation of CuO nanoparticles outside the pores in other images. In some areas of the TEM images, the fringe of the framework of Al-MCM-41 is indefinable. This may be caused by residual surfactant that is not completely removed during the calcination process.

The N_2 adsorption-desorption isotherms of calcined Al-MCM-41 exhibit typical type IV behavior with an H1-type hysteresis loop (Figure 3A(a)), typical for mesoporous materials with two-dimensional hexagonal structures[63]. At the adsorption branch, the adsorbed amount increases gradually as the relative pressure increases because of multilayer adsorption. The small hysteresis loop observed at relative pressures $0.25 \leq P/P_0 \leq 0.4$ may be attributed to the instability of the liquid nitrogen meniscus inside the narrow channels. No obvious hysteresis loop is observed above a relative pressure of 0.9, but a sharp step increase at $P/P_0 = 0.25$–0.40 in the isotherm of the calcined sample reflects both the well-ordered mesoporous structure and the uniformity of the pore size distribution of the sample. The direct-synthesized CuO-Al-MCM-41 sample (Figure 3A(b)) retains the same isotherm shape but the amount of adsorbed nitrogen decreases and the onset of the capillary condensation step shifts to a smaller relative pressure. The decrease of the absorption amount can be attributed to the reduced surface area, whereas the shift of inflection point of the step to lower relative pressure P/P_0 is caused by the smaller pore size, which can be associated with the pore-filling effect because of the incorporation of the CuO nanoparticles into the mesopores of the solid materials[64]. The pore size distribution (Figure 3B (a,b)) calculated from the adsorption branches of the isotherms using BJH model reveals the presence of relatively uniform mesopores in both samples. The BET surface area drops from 1044 m^2/g of Al-MCM-41 to 537 m^2/g of CuO/Al-MCM-41, while the pore volume and pore diameter decrease from 0.91 mL/g and 3.86 nm to 0.67 mL/g and 2.22 nm respectively. As for comparison, the post-synthesized CuO-Al-MCM-41 sample (Figure 3A(c), 3B(c)) almost loses the isotherm shape and uniform pore distribution, indicating that the CuO nanoparticles blocked the mesopores of matrix. The hexagonal (*P6mm* space group) unit cell parameters (α_0; calculated according to the equation $\alpha_0 = 2d_{100}/\sqrt{3}$), BET surface area, and pore volume of the samples are listed in Table 1.

Because peaks corresponding to the CuO phase are not present in the wide-angle XRD pattern of CuO/Al-MCM-41 prepared using copper nitrate as the copper source, XPS is utilized to detect the surface composition and the chemical state of the direct-synthesized CuO/Al-MCM-41 samples using copper chloride and copper nitrate. Signals for Si, O, Al, and Cu are present in the surface analysis of the sample (Figure 4). The Si, Al, and O signals originate from the surface

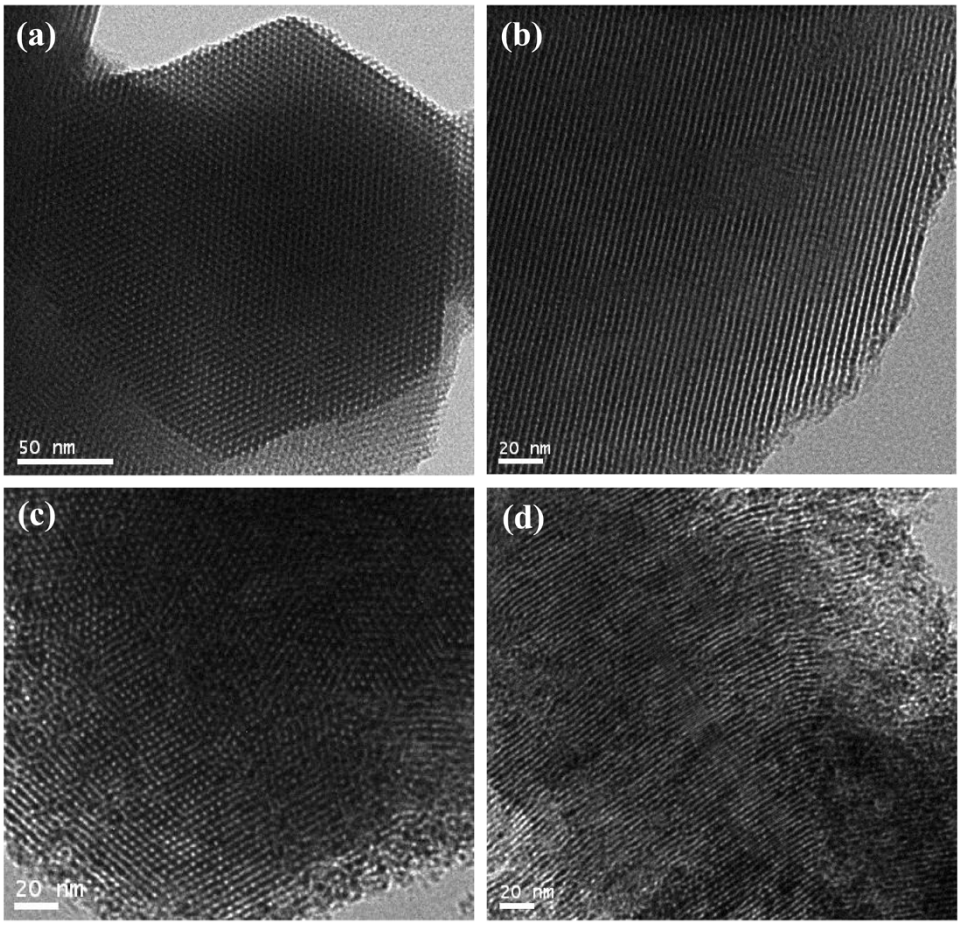

Figure 2 | TEM images of the samples. (a), (b) Al-MCM-41, (c), (d) direct-synthesized CuO/Al-MCM-41: (a), (c) in the direction of the pore axis and (b), (d) in the direction perpendicular to the pore axis, respectively.

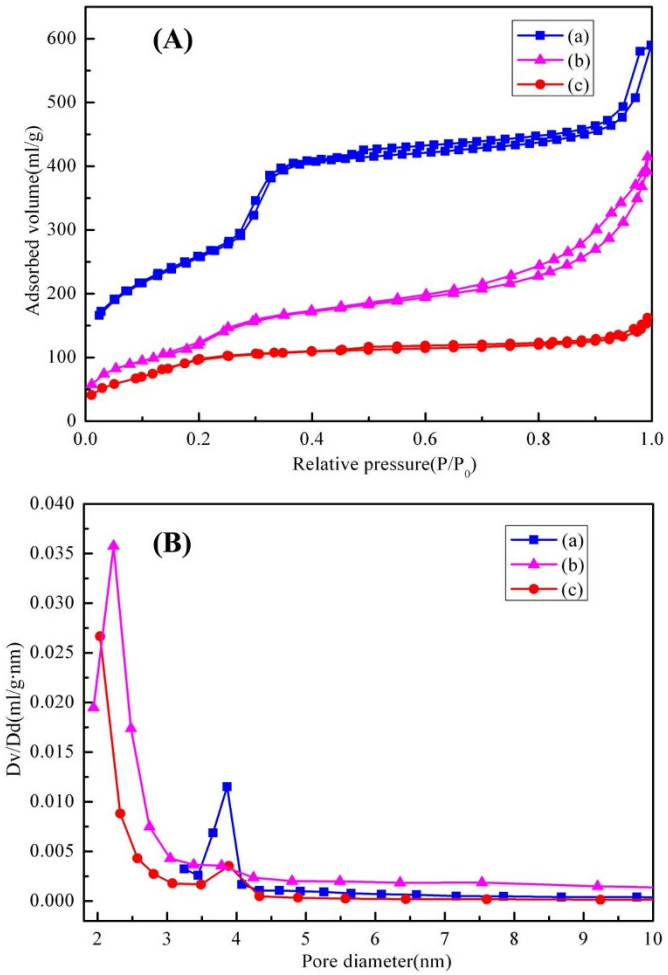

Figure 3 | Porous textures of the samples. (A) N_2 adsorption-desorption isotherms and (B) pore size distribution curves of the samples: (a) Al-MCM-41, (b) direct-synthesized CuO-Al-MCM-41 and (c) post-synthesized CuO/Al-MCM-41 respectively.

of the Al-MCM-41, and the Cu signal originates from the incorporated CuO particles. The high-resolution XPS spectra of the Cu 2p region of the samples synthesized with chloride and nitrate are shown in Figure 4D. The Cu 2p XPS results indicate that the binding energy of the Cu 2p electron in the two samples is almost identical, and the peaks center at approximately 935.7 eV and 955.4 eV, corresponding to $Cu2p_{3/2}$ and $Cu2p_{1/2}$, respectively. The existence of satellite peaks in the spectra suggests that copper exists in the samples as Cu (II). The binding energy value is approximately 935.7 eV, and the binding energy is much greater than that of pure CuO (~933.8 eV), which indicates that the copper atoms are surrounded by silicon[64].

To further study the influence of the CuO particle size on the electronic band gap of the material after encapsulation of CuO nanoparticles, the UV-Vis absorption spectra of different samples are recorded and shown in Figure 5. As expected, the aluminum-containing mesoporous silica (Figure 5a) shows little or no absorbance in the range of 200–700 nm. Bulk CuO nanoparticles (Figure 5d) shows a wide-range absorption between 200 and 700 nm that can be contributed to the characteristic absorption of CuO nanoparticles. The direct-synthesized CuO/Al-MCM-41 (Figure 5b) sample with copper chloride as copper source shows an absorption band at approximately 230 nm that is shifted toward lower wavelengths when compared with the bulk band gap of CuO. Based on TEM observations, the significant shift in the absorption bands is attributed to the encapsulation of CuO nanoparticles inside the mesopores of the material. The blue shift in the absorption maxima of the samples is most likely due to the quantum confinement effect. A similar phenomenon was observed in a previous study[65]. As for the post-synthesized CuO/Al-MCM-41 (Figure 5c), the absorption band is shifted to higher wavelengths, indicating that the CuO nanoparticles might be aggregated and blocked the pores of Al-MCM-41.

In order to investigate the possible bond formation between CuO nanoparticles and Al-MCM-41, FTIR spectra of various samples (Figure 6) were recorded to indicate that the synthesized samples (a) and (b) exhibit absorption bands at approximately 2924, 2855, and 1478 cm^{-1}. These bands correspond to C-H vibrations of the surfactant molecules, and these absorption bands disappear after calcination. The absorption band observed at approximately 3441 cm^{-1} is assigned to the stretching vibrations of -OH units in the adsorbed water, and a band at 3739 cm^{-1} is potentially associated with the asymmetry OH stretching vibrations of silanol groups located at the external surface of the mesoporous materials. For the as-synthesized CuO/Al-MCM-41 sample, the absorption bands at approximately 3545, 3474, and 3241 cm^{-1} are potentially a result of the formation of copper complexes in the silica micelle and template. The Si-OH deformational vibrations of adsorbed molecules produce the absorption band at approximately 1625 cm^{-1}. The absorption band at 1068 cm^{-1}, with a corresponding shoulder at 1227 cm^{-1} and a band at 795 cm^{-1}, are assigned to internal and external asymmetric Si-O stretching modes. These bands are shifted to higher frequencies (1079, 1229, and 802 cm^{-1}) in the calcined samples (Figure 6d). The band at 456 cm^{-1} is attributed to tetrahedral Si-O bending modes, and this band is also slightly shifted to higher wavenumber after calcination. For both the as-synthesized and pure Al-MCM-41 samples (Figure 6c), the band at 965 cm^{-1} corresponds to the stretching vibrations of the surface $Si\text{-}O^-$ groups. This band disappears in the as-synthesized and calcined CuO/Al-MCM-41 samples after introducing the copper species, which could

Table 1 | The textural characteristics of the samples

Samples	d_{110} (nm)	α_0 (nm)	S_{BET} (m^2/g)	V (mL/g)	D_{BJH} (nm)	T (nm)	d (nm)
Al-MCM-41	3.93	4.54	1044	0.91	3.86	0.68	3.86
10CuO/Al-MCM-41(A,d)	3.72	4.30	500	0.57	2.42	1.88	4.53
10CuO/Al-MCM-41(N,d)	3.72	4.30	504	0.63	2.02	2.28	4.98
10CuO/Al-MCM-41(S,d)	3.82	4.41	537	0.67	2.22	2.19	4.98
10CuO/Al-MCM-41(C,d)	3.93	4.54	508	0.64	2.23	2.31	5.05
20CuO/Al-MCM-41(C,d)	3.82	4.41	481	0.77	2.23	2.18	6.43
30CuO/Al-MCM-41(C,d)	3.82	4.41	628	1.07	2.36	2.05	6.81
10CuO/Al-MCM-41(C,p)	3.72	4.30	349	0.25	2.03	2.27	2.88
20CuO/Al-MCM-41(C,p)	3.72	4.30	417	0.27	2.35	1.95	2.60
30CuO/Al-MCM-41(C,p)	3.72	4.30	322	0.22	2.06	2.24	2.70

Notes: α_0-pore parameter ($=2d_{100}/\sqrt{3}$), t-pore wall thickness ($t = \alpha_0 - D_{BJH}$), V-pore volume, d-average pore diameter.
A-acetate, N-nitrate, S-sulfate, C-chloride; d-direct synthesis, p-post synthesis.

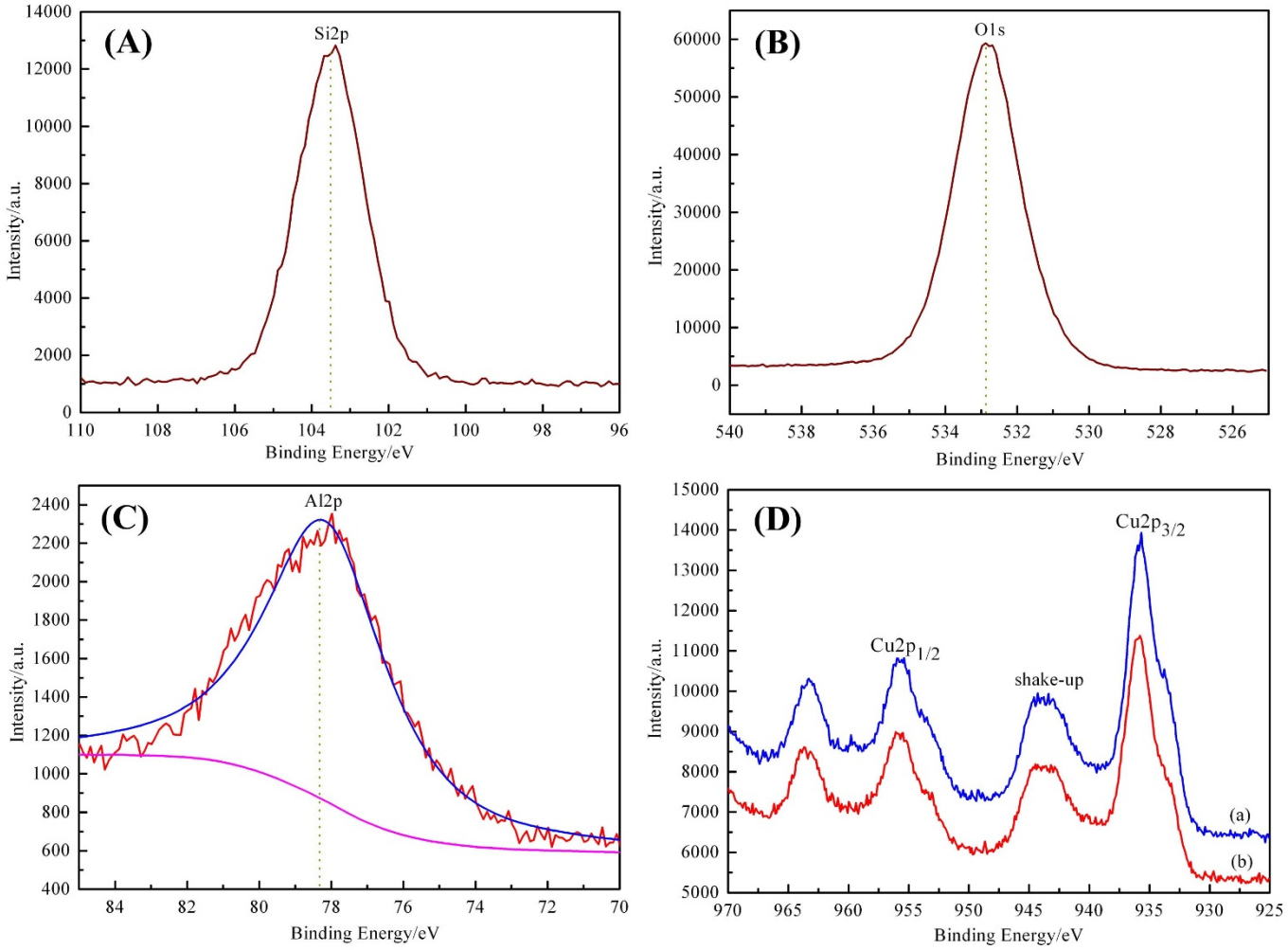

Figure 4 | XPS spectra of the samples. (A) Si 2p, (B) O 1s, (C) Al 2p, and (D) Cu 2p XPS spectra of the direct-synthesized CuO/Al-MCM-41 with different copper sources: (a) chloride and (b) nitrate.

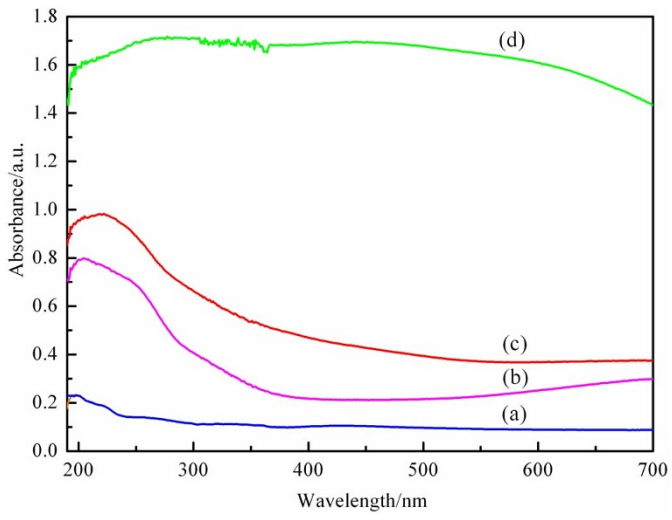

Figure 5 | UV-vis spectra of different samples. (a) Al-MCM-41, (b) direct-synthesized CuO/Al-MCM-41, (c) post-synthesized CuO/Al-MCM-41 and (d) pure CuO.

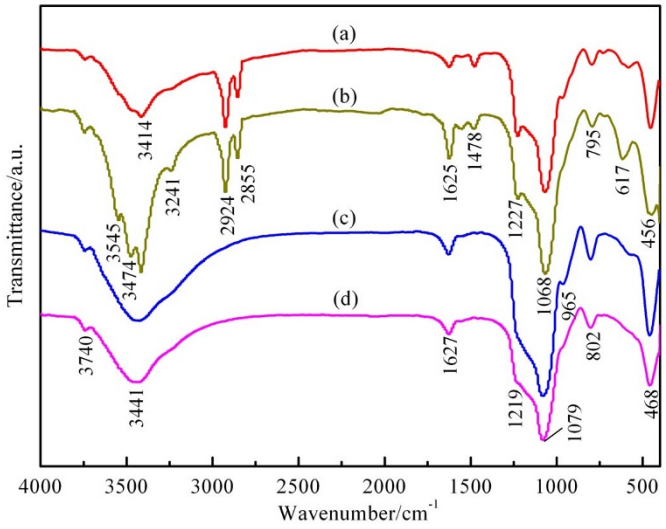

Figure 6 | FTIR spectra of the samples. (a) as-synthesized Al-MCM-41; (b) as-synthesized CuO/Al-MCM-41; (c) Al-MCM-41 and (d) CuO/Al-MCM-41.

be attributed to the interaction between the copper atoms and silicon, such as the formation of Cu-O-Si bonds, consistent with the previous results[66].

Further information about the nature and distribution of CuO within the mesoporous composites can be obtained from H_2-TPR measurements. Figure 7 shows the H_2-TPR profiles of CuO/Al-MCM-41 samples. As for the direct-synthesized samples, a sharp peak with a temperature at maximum reduction T_m at about 215°C and additional shoulder peak centered at about 250°C are observed in Figure 7a. The two hydrogen consumption peaks of copper species in the sample is much lower than that pure CuO with a peak maximum at about 340°C, and the bimodal distribution of H_2-TPR profile of the catalyst contains CuO is consistent with a phenomenon discussed in elsewhere[67]. On the other hand, A broad reduction peak at about 360°C, followed by a poorly defined peak around at 580°C are observed in the post-synthesized sample(Figure 7b), which shift the higher temperature compared that of pure CuO.

According to the previous reported results, the reduction of CuO is easier than the reduction of Cu_2O, further reduction of Cu^+ to Cu^0 requires a higher temperature and apparent activation energy, and CuO powders reduce to metallic Cu instead of an intermediate phase, such as Cu_2O or Cu_4O_3[68]. Taking into account the general dependence of T_m on the particles size, i.e. smaller particles are expected to be reduced at lower temperature, the two hydrogen consumption peaks in the direct-synthesized sample can be ascribed to reduction of the fine CuO particles highly dispersed at the internal surface of the mesoporous composite (at 215°C) and somewhat larger CuO clusters at the pore surface (at 250°C), respectively. The T_m (at 215°C) value of the reduction process agrees with the previous TPR studies of copper-containing mesoporous silica materials, and the results may be clearly interpreted as indicating that mainly of the CuO nanoparticles are embedded in the mesoporous structure of the composite[58]. It is worth mentioning that the Al-containing mesoporous materials in our results have the higher thermal stability than the pure silica mesoporous materials. And similarly, reduction peaks at higher temperature in the post-synthesized sample is corresponded to the reduction of supported CuO aggregates anchored on the external surface with a larger particle size. It can be concluded that the nanoparticles are liable to incorporate into the pore channel of the mesoporous materials through direct-synthesis method, which can effectively avoid the formation of blocked channels that commonly arise in the post-synthesis method, and then provide a relatively high specific surface area. It is confirmed that the direct-synthesized samples have higher BET specific surface area than that of the post-synthesized samples. Therefore, it is possible to expect that other metal oxides or metals can be encapsulated into the mesoporous structures by the direct synthetic method.

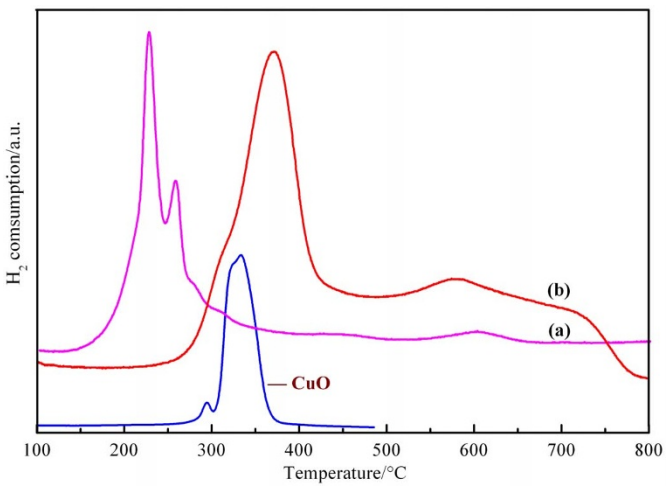

Figure 7 | H_2-TPR profiles of CuO/Al-MCM-41 samples. (a) direct-synthesized; (b) post-synthesized.

Discussion

We in detail investigated the effects of different copper sources on the structure, morphology and porous parameters of CuO/Al-MCM-41 samples. A series of XRD patterns for the CuO/Al-MCM-41 samples prepared with different copper sources using a direct-synthetic technique are shown in Figure S1. All of the samples in Figure S1A exhibit three diffraction patterns characteristic of mesoporous silica monoliths, which suggests that the samples have good long-range order. The diffraction peaks can be indexed to the (100), (110), and (200) diffractions associated with a typical two-dimensional hexagonal symmetry (*P6mm*). However, when compared with the pure Al-MCM-41 sample (Figure 1A(b)), the intensities of these characteristic diffraction peaks decrease after the incorporation of the CuO nanoparticles. The (210) peak is too weak to observe, possibly due to the incorporation of copper oxide into the framework of Al-MCM-41 and the concomitant decrease of order in the structure. The wide-angle XRD patterns for these samples are shown in Figure S1B. In the region of $2\theta = 10°–80°$, the broad peak at approximately 23° results from the diffraction of the amorphous SiO_2 walls of Al-MCM-41. In samples (a), (b), and (d), three distinct diffraction peaks appeared at $2\theta = 35.4°$, 38.8° and 49.8°, which can be indexed to the (002), (111), and ($\bar{2}$02) diffractions for CuO phase respectively. These features are absent in sample (c), which may be attributed to the formation of small or amorphous particles inside the composites. The corresponding TEM images (Figure S2) also indicate that the fringe of the framework of Al-MCM-41 is indefinable, and that small CuO nanoparticles could be incorporated within the mesopores of Al-MCM-41 without CuO nanocrystals deposited onto the mesoporous composites. Further N_2 adsorption-desorption isotherms and pore size distribution elucidate that four samples exhibit isotherms similar in overall shape (Figure S3, Table 1). The isotherms are type IV with a H1 hysteresis loop, characteristic of mesoporous materials with two-dimensional hexagonal structures (Figure S3A). Figure S3B shows a narrow pore size distribution centered at a diameter of 2–2.4 nm.

Furthermore, we discuss the effects of content of loaded CuO in CuO/Al-MCM-41 prepared by directly adding specific amounts of metal precursors (here, copper chloride was utilized) into the starting sols using the direct synthetic technique. The intensity of the (100) diffraction peak decreases significantly as the doping of the initial reaction composition increase, suggesting that the long-range regularity of the material's mesostructure decreased as more CuO was incorporated into the material (Figure S4A). Even when the mass ratio of CuO to silicon is as high as 0.3, three well-resolved diffraction peaks that are indexed to the (100), (110), and (200) diffractions can still be observed for the doped mesoporous silica monoliths. The WAXRD patterns (Figure S4B) show well-resolved diffraction peaks for the CuO nanocrystals due to the confined geometry provided by the channels of the mesoporous silica that segregate CuO particles and restrain the particle's growth. A similar phenomenon has also been observed in other nanoparticle-loaded mesoporous silica[37,56,69].

The corresponding TEM images show that the mesoporous structure typical of Al-MCM-41 materials was maintained when CuO nanoparticles were incorporated using the direct synthetic method (Figure S5). Some disorganized worm-like structures were observed in the fringe of the framework. Both ordered one-dimensional straight channels and hexagonal pores are observed. Increasing CuO loading results in mesoporous particles with an increased number of CuO nanoparticles or clusters. Increasing the amount of CuO does not significantly deteriorate the structure of the mesoporous materials. Figure S6 displays both the N_2 sorption isotherms and the pore size distributions of the CuO/Al-MCM-41 samples with 10, 20, and

30 wt% of CuO. All samples have a type-IV isotherm featuring a slight increase of capillary condensation at relative pressure $P/P_0 \geq 0.25$, which is characteristic of mesoporous materials with uniform size distribution. The structural parameters are summarized in Table 1. Interestingly, the volume of nitrogen adsorbed increases with an increase in CuO loading. The pore size distribution (Figure S6B) exhibits sharp peaks for all samples, indicating that all samples have uniform pore sizes. The pore size for these samples remains at ~2.30 nm, which is smaller than that of the pure Al-MCM-41. The decrease in pore diameter results from the partial filling of the pores with CuO or from an alteration of the assembled structure at high ionic strength. A high CuO loading may also decrease the silica network strength and connectivity, which would result in smaller pores because of an increase in pore shrinkage during calcination[70].

For comparison, mesoporous composites with various CuO loadings (10, 20, and 30 wt%) were also prepared by the post-synthetic method. The (100), (110) and (200) diffraction peaks are well resolved in Figure S7A, indicating that the highly ordered hexagonal structure typical of MCM-41 materials was retained after the grafting reaction. The *d*-spacings for the first diffraction peaks of these samples do not shift with increasing amount of CuO, and the mesostructured regularity does not decrease. WXRD patterns show that CuO crystallites are present in these samples (Figure S7B). Three peaks (2θ values of 35.4°, 38.8° and 49.8°) and six other peaks with relatively low intensities are present in sample b, c, indicating a poorer dispersion of copper oxide in this sample. N_2 sorption properties provide further evidence that the mesostructure was maintained after incorporating CuO nanoparticles using a post-synthesis route. The three samples exhibit isotherms with similar shapes (Figure S8A), while the amount of adsorbed nitrogen is much less than that of pure Al-MCM-41. The pore size distribution curves (Figure S8B) exhibit a smaller peak centered at approximately 4.0 nm, which probably correlates to the size of the interparticle pore. These results suggest that the CuO nanoparticles may form on the external surface of the parent Al-MCM-41. As shown in Table 1, the significantly decreased BET surface area and pore volume of these samples also imply that the pores of the samples are partially blocked. The composites prepared by the direct-synthetic method possess an improved mesostructure, have a larger surface area and pore volume than those by the post-synthetic method (Table 1). These results prove that CuO nanoparticles were confined in the pores of Al-MCM-41 through the direct synthetic method. Therefore, this direct synthetic method may be a facile and effective way to produce high surface areas and loadings for the encapsulation of metal oxides and metals into mesoporous materials.

In summary, a highly ordered Al-MCM-41 mesoporous material with BET surface area of 1044 m^2/g, pore volume of 0.91 cm^3/g and average pore size of 3.86 nm has been successfully synthesized using leached attapulgite as the Si and Al source. CuO/Al-MCM-41 samples were prepared using a facile and effective direct synthetic method by the incorporation of CuO nanoparticles into the Al-MCM-41 matrix. The as-synthesized mesoporous composites showed a relatively high BET surface area and improved thermal stability compared with pure Al-MCM-41. The absorption edge of the copper oxide in the mesoporous materials exhibited a blue shift, which was attributed to the quantum confinement effect because of the encapsulation of CuO nanoparticles inside the mesopores. H_2-TPR results demonstrated that the reduction peaks of the direct synthesized sample happened at temperature much lower than that of the post-synthesized sample due to the smaller particle size, indicating that the CuO nanoparticles were encapsulated in the pores of the mesoporous composite. This direct synthesis can potentially be utilized to prepare mesoporous materials containing metal oxides and transition metal nanoparticles by using leached silicate minerals as Si source. These composite materials have potentially extensive applications in catalysis.

Methods

Synthesis of pure Al-MCM-41. Al-MCM-41 was prepared according to literature procedures with small modifications[32]. In a typical synthesis, 10.0 g of attapulgite (ground at 600 rpm for 2 h) was first mixed with 15 g of solid NaOH (A.R.). This mixture was heated at 600°C for 2 h and was subsequently dispersed in 400 mL of deionized water by stirring and then aged at room temperature for 16 h. The supernatant was used as the Si and Al source without the addition of Si or Al reagents. 1.0 g of cetyltrimethylammonium bromide (CTAB, A.R.) and 1.0 g of polyethylenglycol 4000 (PEG4000, A.R.) were dissolved in 50 mL of deionized water, and 80 mL of supernatant was then dropped into this solution while the solution was stirred. This mixture was vigorously stirred for 1 h at 30°C. A HCl solution (2 M) was added dropwise to adjust the pH value of the mixture to 9.0. After pH adjustment, the white mixture was stirred at 30°C for 1 h in a water bath and was transferred into a Teflon-lined steel autoclave. The sample was statically heated at 110°C for 24 h and then cooled to room temperature. The resultant product was filtered, washed and dried at 80°C for 12 h to produce the as-synthesized sample. The sample was calcined at a heating rate of 2°C/min to 550°C and maintained at this temperature for 4 h to remove the template and produce the white powder of Al-MCM-41.

Direct-synthesis of CuO/Al-MCM-41. The synthetic procedure used to produce CuO/Al-MCM-41 composites was similar to the synthesis of the Al-MCM-41 material. The difference is that $CuCl_2 \cdot 2H_2O$ dissolved in deionized water with CTAB was added to the white mixture before the mixture was transferred into the Teflon-lined steel autoclave. The pH value of the light-blue mixture was maintained at 9.0 and stirred at 30°C for 1 h. The subsequent steps were the same as those used to in the synthesis Al-MCM-41. The obtained powders were denoted as CuO/Al-MCM-41 after calcination at 550°C.

Post-synthesis of CuO/Al-MCM-41. To produce CuO/Al-MCM-41 using a post-synthesis method, various amounts of copper chloride were dissolved in deionized water and stirred uniformly. Subsequently, 0.5 g of Al-MCM-41 was immersed into the above solution with different concentrations of Cu^{2+} by ultrasound for 15 min, and this solution was stirred for 6 h. The pH value of the mixture was adjusted to 8.0 by adding a NaOH solution (0.1 M) to the vigorous stirred solution. The gel mixture was stirring for 6 h and aged for 10 h. The resulting product was filtered, washed with deionized water several times, and dried at 80°C overnight. Finally, the powder mixture was calcined at 550°C for 2 h to produce the CuO/Al-MCM-41 composites.

Characterization. X-ray diffraction (XRD) patterns of the materials were collected on a D8 Advance Bruker diffractometer using Cu Kα radiation (λ = 1.5406 Å). Transmission electron microscopy (TEM) studies were conducted on a JEOL JEM-2100F microscope operating at 200 kV with a tungsten filament. Samples were prepared by suspending CuO/Al-MCM-41 composites in ethanol followed by sonication for 15 min in an ultrasonic bath. The suspension was dropped onto a copper grid and allowed to dry. Nitrogen gas adsorption-desorption isotherms were measured at 77 K using a Micromeritics ASAP 2020 Sorptometer. Prior to adsorption, the samples were vacuum-dried at 200°C for 10 h. The Brunauer-Emmett-Teller (BET) specific surface area was calculated using adsorption data in the relative pressure range of 0.04–0.2, and the total pore volume was obtained from the amount adsorbed at a relative pressure of approximately 0.99. The pore size distribution curves were calculated from the analysis of the desorption branch of the isotherm using the Barrett-Joyner-Halenda (BJH) algorithm. X-ray photoelectron spectroscopy (XPS) measurements were performed on a Thermo Fisher Scientific K-Alpha 1063 spectrophotometer using Al Kα radiation. The materials were compressed into pellets prior to XPS measurements. FT-IR spectra of the samples were collected on a Nicolet Nexus 670 FT-IR spectrometer in the range of 4000–400 cm^{-1} using KBr discs. Ultraviolet-visible (UV-vis) spectrophotometry spectra were collected on a TU-1901 spectrophotometer at room temperature, and the detection range of the spectrophotometer is 190 nm to 700 nm. Hydrogen temperature programmed reduction (H_2-TPR) measurements were performed utilizing a FINESORB-3010 under a flow of 10% H_2/Ar gas mixture and a heating rate of 10°C/min from room temperature to 800°C. Before the TPR analysis, the carbonates and hydrates impurities were removed by flowing argon over the catalyst at a flow rate of 30 mL/min at 300°C for 1 h, and then the system was cooled to room temperature. The amount of H_2 uptake during the reduction was measured continuously with a thermal conductivity detector (TCD).

1. Kresge, C. T. *et al.* Ordered mesoporous molecular sieves synthesized by a liquid crystal template mechanism. *Nature* **359**, 710–712 (1992).
2. Beck, J. S. *et al.* A new family of mesoporous molecular sieves prepared with liquid crystal templates. *J. Am. Chem. Soc.* **114**, 10834–10843 (1992).
3. Wu, Z. *et al.* Multiple functionalization of mesoporous silica in one-pot: direct synthesis of aluminum-containing plugged SBA-15 from aqueous nitrate solutions. *Adv. Funct. Mater.* **18**, 82–94 (2008).
4. Luan, Z., Cheng, C., Zhou, W. & Klinowski, J. Mesopore molecular sieve MCM-41 containing framework aluminum. *J. Phys. Chem.* **99**, 1018–1024 (1995).
5. Zhang, Z. *et al.* Mesoporous aluminosilicates with ordered hexagonal structure, strong acidity, and extraordinary hydrothermal stability at high temperatures. *J. Am. Chem. Soc.* **123**, 5014–5021 (2001).

6. Corma, A. From microporous to mesoporous molecular sieve materials and their use in catalysis. *Chem. Rev.* **97**, 2373–2419 (1997).
7. Han, Y. *et al.* A novel method for incorporation of heteroatoms into the framework of ordered mesoporous silica materials synthesized in strong acidic media. *J. Phys. Chem. B* **105**, 7963–7966 (2001).
8. Schumacher, K. *et al.* The synthesis of spherical mesoporous molecular sieves MCM-48 with heteroatoms incorporated into the silica framework. *Adv. Mater.* **11**, 1194–1198 (1999).
9. Mokaya, R. Ultrastable mesoporous aluminosilicates by grafting routes. *Angew. Chem. Int. Ed.* **38**, 2930–2934 (1999).
10. Zhao, X. S., Lu, G. Q. (M.). & Millar, G. J. Advances in mesoporous molecular sieve MCM-41. *Ind. Eng. Chem. Res.* **35**, 2075–2090 (1996).
11. Ryoo, R., Ko, C. H. & Howe, R. F. Imaging the distribution of framework aluminum in mesoporous molecular sieve MCM-41. *Chem. Mater.* **9**, 1607–1613 (1997).
12. Mokaya, R. Synthesis of mesoporous aluminosilicates with enhanced stability and ion- exchange capacity via a secondary crystallization route. *Adv. Mater.* **12**, 1681–1685 (2000).
13. Liu, Y., Zhang, W. & Pinnavaia, T. J. Steam-stable MSU-S aluminosilicate mesostructures assembled from zeolite ZSM-5 and zeolite beta seeds. *Angew. Chem. Int. Ed.* **40**, 1255–1258 (2001).
14. O'Neil, A. S., Mokaya, R. & Poliakoff, M. Supercritical fluid-mediated alumination of mesoporous silica and its beneficial effect on hydrothermal stability. *J. Am. Chem. Soc.* **124**, 10636–10637 (2002).
15. Liu, Y., Zhang, W. & Pinnavaia, T. J. Steam-stable aluminosilicate mesostructures assembled from zeolite type Y seeds. *J. Am. Chem. Soc.* **122**, 8791–8792 (2000).
16. Mokaya, R. & Jones, W. Aluminosilicate mesoporous molecular sieves with enhanced stability obtained by reacting MCM-41 with aluminium chlorohydrate. *Chem. Commun.* 1839–1840 (1998).
17. Ryoo, R., Jun, S., Kim, J. M. & Kim, M. J. Generalised route to the preparation of mesoporous metallosilicates *via* post-synthetic metal implantation. *Chem. Commun.* 2225–2226 (1997).
18. Mokaya, R. Influence of pore wall thickness on the steam stability of Al-grafted MCM-41. *Chem. Commun.* 633–634 (2001).
19. Mokaya, R. & Jones, W. Post-synthesis grafting of Al onto MCM-41. *Chem. Commun.* 2185–2186 (1997).
20. Pauly, T. R. *et al.* Textural mesoporosity and the catalytic activity of mesoporous molecular sieves with wormhole framework structures. *J. Am. Chem. Soc.* **121**, 8835–8842 (1999).
21. Janicke, M. T. *et al.* Low silica MCM-41 composites and mesoporous solids. *Chem. Mater.* **11**, 1342–1351 (1999).
22. Vinu, A., Murugesan, V., Böhlmann, W. & Hartmann, M. An optimized procedure for the synthesis of AlSBA-15 with large pore diameter and high aluminum content. *J. Phys. Chem. B* **108**, 11496–11505 (2004).
23. Biz, S. & White, M. G. Syntheses of aluminosilicate mesostructures with high aluminum content. *J. Phys. Chem. B* **103**, 8432–8442 (1999).
24. Zhang, Z. *et al.* Strongly acidic and high-temperature hydrothermally stable mesoporous aluminosilicates with ordered hexagonal structure. *Angew. Chem. Int. Ed.* **40**, 1258–1262 (2001).
25. Liu, Y. & Pinnavaia, T. J. Assembly of hydrothermally stable aluminosilicate foams and large-pore hexagonal mesostructures from zeolite seeds under strongly acidic conditions. *Chem. Mater.* **14**, 3–5 (2002).
26. Li, W., Huang, S. J., Liu, S. B. & Coppens, M. O. Influence of the Al source and synthesis of ordered Al-SBA-15 hexagonal particles with nanostairs and terraces. *Langmuir* **21**, 2078–2085 (2005).
27. Yang, X. Y. *et al.* A highly ordered mesoporous aluminosilicate, CMI-10, with a Si/Al ratio of one. *Adv. Mater.* **18**, 2117–2122 (2006).
28. Li, Y., Yang, Q., Yang, J. & Li, C. Mesoporous aluminosilicates synthesized with single molecular precursor $(sec\text{-}BuO)_2AlOSi(OEt)_3$ as aluminum source. *Micropor. Mesopor. Mater.* **91**, 85–91 (2006).
29. Kimura, T. & Kuroda, K. Ordered mesoporous silica derived from layered silicates. *Adv. Funct. Mater.* **19**, 511–527 (2009).
30. Yanagisawa, T., Shimizu, T., Kuroda, K. & Kato, C. The preparation of alkyltrimethyl- ammonium-kanemite complexes and their conversion to microporous materials. *Bull. Chem. Soc. Jpn.* **63**, 988–992 (1990).
31. Linssen, T. *et al.* Physicochemical and structural characterization of mesoporous aluminosilicates synthesized from leached saponite with additional aluminum incorporation. *Chem. Mater.* **15**, 4863–4873 (2003).
32. Yang, H., Deng, Y., Du, C. & Jin, S. Novel synthesis of ordered mesoporous materials Al-MCM-41 from bentonite. *Appl.Clay Sci.* **47**, 351–355 (2010).
33. Wang, G. *et al.* Synthesis of highly regular mesoporous Al-MCM-41 from metakaolin. *Appl. Clay Sci.* **44**, 185–188 (2009).
34. Yang, H. *et al.* Enhanced photoluminescence property of SnO_2 nanoparticles contained in mesoporous silica synthesized with leached talc as Si source. *Micropor. Mesopor. Mater.* **102**, 204–211 (2007).
35. Yang, H. *et al.* From natural attapulgite to mesoporous materials: methodology, characteri- zation and structural evolution. *J. Phys. Chem. B* **114**, 2390–2398 (2010).
36. Kato, M., Shigeno, T., Kimura, T. & Kuroda, K. Influence of the kind of layered disodium disilicates on the formation of silica-organic mesostructured materials. *Chem. Mater.* **16**, 3224–3230 (2004).
37. Wang, S., Choi, D. G. & Yang, S. M. Incorporation of CdS nanoparticles inside ordered mesoporous silica SBA-15 via ion exchange. *Adv.Mater.* **14**, 1311–1314 (2002).
38. Zhang, W. H. *et al.* Synthesis and characterization of bifunctionalized ordered mesoporous materials. *Adv. Funct. Mater.* **14**, 544–552 (2004).
39. Gao, F., Lu, Q. & Zhao, D. Synthesis of crystalline mesoporous CdS semiconductor nanoarrays through a mesoporous SBA-15 silica template technique. *Adv. Mater.* **15**, 739–742 (2003).
40. Parala, H. *et al.* Confinement of CdSe nanoparticles inside MCM-41. *Adv. Mater.* **12**, 1050–1055 (2000).
41. Gao, F. *et al.* Controlled synthesis of semiconductor PbS nanocrystals and nanowires inside mesoporous silica SBA-15 phase. *Nano Lett.* **1**, 743–748 (2001).
42. Krishnan, C. K., Hayashi, T. & Ogura, M. A new method for post-synthesis coating of zirconia on the mesopore walls of SBA-15 without pore blocking. *Adv. Mater.* **20**, 2131–2136 (2008).
43. Hess, D. M. *et al.* Fabrication of ordered mesoporous silica films with encapsulated iron oxide nanoparticles using ferritin-doped block copolymer templates. *Chem. Mater.* **21**, 2125–2129 (2009).
44. Tian, B. *et al.* General synthesis of ordered crystallized metal oxide nanoarrays replicated by microwave digested mesoporous silica. *Adv. Mater.* **15**, 1370–1374 (2003).
45. Zhu, K., Yue, B., Zhou, W. & He, H. Preparation of three-dimensional chromium oxide porous single crystals templated by SBA-15. *Chem. Commun.* 98–99 (2003).
46. Wang, Y. M., Wu, Z. Y., Wang, H. J. & Zhu, J. H. Fabrication of metal oxides occluded in ordered mesoporous hosts via a solid-state grinding route: the influence of host–guest interactions. *Adv. Funct. Mater.* **16**, 2374–2386 (2006).
47. Li, Y. *et al.* Iron-functionalized Al-SBA-15 for benzene hydroxylation. *Chem. Commun.* 774–776 (2008).
48. Yamamoto, K., Sunagawa, Y., Takahashi, H. & Muramatsu, A. Metallic Ni nanoparticles confined in hexagonally ordered mesoporous silica material. *Chem. Commun.* 348–350 (2005).
49. Knya, Z. *et al.* Nanocrystal templating of silica mesopores with tunable pore sizes. *Nano Lett.* **2**, 907–910 (2002).
50. Liong, M., France, B., Bradley, K. A. & Zink, J. I. Antimicrobial activity of silver nanocrystals encapsulated in mesoporous silica nanoparticles. *Adv. Mater.* **21**, 1684–1689 (2009).
51. Yang, C., Sheu, H. & Chao, K. Templated synthesis and structural study of densely packed metal nanostructures in MCM-41 and MCM-48. *Adv. Funct. Mater.* **12**, 143–148 (2002).
52. Liu, Z. *et al.* TEM studies of platinum nanowires fabricated in mesoporous silica MCM-41. *Angew. Chem. Int. Ed.* **39**, 3107–3110 (2000).
53. Jones, M. D. *et al.* Solid-state NMR studies of MCM-41 supported with a highly catalytically active cluster. *Angew. Chem. Int. Ed.* **41**, 4726–4729 (2002).
54. Song, H. *et al.* Hydrothermal growth of mesoporous SBA-15 silica in the presence of PVP-stabilized Pt nanoparticles: synthesis, characterization, and catalytic properties. *J. Am. Chem. Soc.* **128**, 3027–3037 (2006).
55. Yacou, C. *et al.* One pot synthesis of hierarchical porous silica membrane material with dispersed Pt nanoparticles using a microwave-assisted sol-gel route. *J. Mater. Chem.* **18**, 4274–4279 (2008).
56. Yang, X. Y. *et al.* One-pot synthesis of catalytically stable and active nanoreactors: encapsulation of size-controlled nanoparticles within a hierarchically macroporous core@ordered mesoporous shell system. *Adv. Mater.* **21**, 1368–1372 (2009).
57. Andersson, N., Corkery, R. W. & Alberius, P. C. A. One-pot synthesis of well ordered mesoporous magnetic carriers. *J. Mater. Chem.* **17**, 2700–2705 (2007).
58. Derrien, G. *et al.* Copper-containing monodisperse mesoporous silica nanospheres by a smart one-step approach. *Chem. Commun.* 3118–3120 (2008).
59. Yang, H. *et al.* One-step synthesis of highly ordered mesoporous silica monoliths with metal oxide nanocrystals in their channels. *Adv. Funct. Mater.* **15**, 1377–1384 (2005).
60. Zhang, W. *et al.* Hierarchical self-assembly of microscale cog-like superstructures for enhanced performance in lithium-ion batteries. *Adv. Funct. Mater.* **21**, 3516–3523 (2011).
61. Gao, X. P. *et al.* Preparation and electrochemical performance of polycrystalline and single crystalline CuO nanorods as anode materials for Li ion battery. *J. Phys. Chem. B* **108**, 5547–5551 (2004).
62. Zhou, M. *et al.* Carbonate-assisted hydrothermal synthesis of nanoporous CuO microstructures and their application in catalysis. *Eur. J. Inorg. Chem.* **2010**, 729–734 (2010).
63. Zhao, D. *et al.* Triblock copolymer syntheses of mesoporous silica with periodic 50 to 300 angstrom pores. *Science* **279**, 548–552 (1998).
64. Gierszal, K. P., Yoon, S. B., Yu, J. S. & Jaroniec, M. Adsorption and structural properties of mesoporous carbons obtained from mesophase pitch and phenol-formaldehyde carbon precursors using porous templates prepared from colloidal silica. *J. Mater. Chem.* **16**, 2819–2823 (2006).
65. Wang, Y. M., Wu, Z. Y., Shi, L. Y. & Zhu, J. H. Rapid functionalization of mesoporous materials: directly dispersing metal oxides into as-prepared SBA-15 occluded with template. *Adv. Mater.* **17**, 323–327 (2005).
66. Kong, Y. *et al.* Investigation of the structure of MCM-41 samples with a high copper content. *Adv. Funct. Mater.* **14**, 816–820 (2004).

67. Kargol, M. *et al.* Copper- and silver-containing monolithic silica-supported preparations for selective propene-propane adsorption from the gas phase. *Chem. Mater.* **17**, 6117–6127 (2005).
68. Kim, J. Y. *et al.* Reduction of CuO and Cu_2O with H_2: H embedding and kinetic effects in the formation of suboxides. *J. Am. Chem. Soc.* **125**, 10684–10692 (2003).
69. Alvaro, M., Aprile, C., Garcia, H. & Gómez-García, C. J. Synthesis of a hydrothermally stable, periodic mesoporous material containing magnetite nanoparticles, and the preparation of oriented films. *Adv. Funct. Mater.* **16**, 1543–1548 (2006).
70. Hampsey, J. E., Arsenault, S., Hu, Q. & Lu, Y. One-step synthesis of mesoporous metal-SiO_2 particles by an aerosol-assisted self-assembly process. *Chem. Mater.* **17**, 2475–2480 (2005).

Acknowledgments

This work was supported by the National Science Fund for Distinguished Young Scholars (51225403), the Specialized Research Fund for the Doctoral Program of Higher Education (20120162110079) and Hunan Provincial Innovation Foundation for Postgraduates (CX2011B120).

Author contributions

H.M.Y. conceived the project and wrote the final paper. C.L.H. designed the experiments, synthesized and characterized the materials, and wrote initial drafts of the work. H.M.Y., C.L.H. and J.O.Y. analyzed the data. All authors discussed the results and commented on the manuscript.

Additional information

Supplementary information accompanies this paper at http://www.nature.com/scientificreports

Competing financial interests: The authors declare no competing financial interests.

How to cite this article: Huo, C.L., Ouyang, J. & Yang, H.M. CuO nanoparticles encapsulated inside Al-MCM-41 mesoporous materials via direct synthetic route. *Sci. Rep.* **4**, 3682; DOI:10.1038/srep03682 (2014).